Causal Artificial Intelligence Counterfactual Prediction of Material's Superconducting Critical Temperature

Ž. Kurtanjek*
Faculty of Food Technology and Biotechnology
University of Zagreb, Croatia

doi: https://doi.org/10.15255/CABEQ.2025.2466
Original scientific paper
Received: November 20, 2025
Accepted: April 27, 2026

A causal artificial intelligence (AI) model was developed to support the discovery of new superconducting materials by analysing causal relationships between interval-valued elemental descriptors and the superconducting critical temperature, T_c. The aim is to explore a broad elemental composition space without requiring prior knowledge of material structure. Using a University of California, Irvine dataset comprising 21,263 materials with chemical formulae, 81 features, and T_c values were aggregated into temperature-based intervals and analysed within a reproducing kernel Hilbert space framework to infer a causal directed acyclic graph. Three interval features emerged as direct causal drivers of T_c: the standard deviation of mass density, the weighted geometric mean of electron affinity, and the weighted geometric mean of valence. A random forest model using all predictors achieved an R^2 of approximately 92.9 %, while the causal model, using only these three features, achieved an R^2 of approximately 89.7 %. Under out-of-distribution splits, the causal model demonstrated superior robustness. Estimated interventional ("do") effects revealed nonlinear behaviour, and counterfactual analyses of hypothetical interventions further demonstrated the potential of causal AI for guiding exploration of new materials.

Key words
superconductivity, causality, counterfactual, Bayes network, reproducing kernel Hilbert space

Introduction

Recently, three physicists—J. Clarke, M. Devoret, and J. Martinis—were awarded the 2025 Nobel Prize in Physics for their contributions to understanding how quantum physics at macroscopic scales gives rise to the electrical superconductivity phenomenon[1].

The superconductivity phenomenon was first discovered in 1911 by Dutch physicist Heike Kamerlingh Onnes, who observed that mercury becomes superconducting at 4.2 K. For this discovery, he received the 1913 Nobel Prize in Physics[2]. Since then, numerous superconducting materials have been identified, and several theoretical frameworks have been developed to explain the underlying physics. Nevertheless, superconductivity remains a central topic in both theoretical and experimental physics. Key milestones include the development of the Bardeen–Cooper–Schrieffer theory of conventional superconductivity in the 1950s and the discovery of the first high-temperature superconductors in the 1980s. More recently, unconventional superconductivity has been demonstrated in twisted bilayer graphene, and claims of room-temperature superconductivity have generated intense debate[3].

The rapid expansion of generative artificial intelligence (AI) technologies has intensified the demand for advances in superconducting materials. It is estimated that by 2040, nearly 50 % of global electricity consumption may be attributable to computing. Power consumption and heat dissipation in large-scale data centres are emerging as major constraints, with substantial energy losses as waste heat posing a significant barrier to the continue development of AI-driven data centres. In modern data centres, roughly 40 % of total electrical energy is dissipated as low-grade heat due to cooling requirements—losses that could be significantly reduced through superconducting infrastructure. Superconductors offer a promising route to dramatically reducing energy consumption, as they allow the current to flow without dissipating into heat. Superconducting materials therefore have the potential to transform data centre efficiency by eliminating resistive losses in power distribution and computing hardware, reducing heat generation, and enabling ultrafast, low-power data processing[4,5].

*Corresponding author: zelimir.kurtanjek@gmail.com

The complexity and intrinsic difficulty of discovering industrially viable superconducting materials have motivated extensive use of AI-based modelling. Numerous studies have applied machine-learning algorithms to model the dependence of the superconducting critical temperature (T_c) on material properties. For example, a Random Forest model based on features extracted from chemical formulae achieved an untrained prediction error of ±9.5 K using the chemical composition of 34,000 samples from the SuperCon dataset. When applied with singular value decomposition, a "bagged tree" variant of the Random Forest model achieved the highest accuracy, with R^2 = 0.93 [6,7]. A Bayesian neural network trained solely on chemical composition captured relevant correlations and improved interpretability, reaching R^2 = 0.940 with a root mean square error (RMSE) of 3.83 K [8]. A suite of regularised linear models, including Ridge, Lasso, Elastic Net, and the spline-based nonparametric Multivariate Adaptive Regression Splines (MARS) method, yielded mean absolute error (MAE) values of 10.75, 14.50, 13.43, and 13.44 K, respectively, for untrained data, underscoring the importance of nonlinear interactions[9]. A Gradient-Boosted Feature Selection (GBFS) workflow tailored for T_c prediction, using a distributed gradient-boosting framework, achieved R^2 = 0.94 and MAE = 3.73 K during 10-fold cross-validation[10]. An extensive comparative study evaluated methods including AdaBoost, Kernel Ridge, Linear Regression, Lasso-Lars, Linear Support Vector Regression, Multi-Layer Perceptron, Random Forest, Stochastic Gradient Descent, and XGBoost. For untrained data, Extreme Gradient Boosting (XGBoost) delivered the best accuracy with a median RMSE = 9.4 K. In out-of-domain prediction, the spline continued-fraction regressor performed with median RMSE = 36.3 K [11], a stacked ensemble of models (Ridge, Lasso, KNN, MLP, SVR) achieved RMSE = 9.68 K, R^2 = 0.922, MAE = 5.38 K, and MAPE = 4.57 % [12]. Using XGBoost, R^2 = 0.924 and RMSE = 9.336 K (via 10-fold cross validation) were obtained, with thermal-conductivity range, weighted geometric mean of thermal conductivity, and atomic-radius range identified as the most influential features[13]. The effect of pressure, an essential factor influencing crystalline structure, electronic structure, lattice dynamics, and ultimately Cooper-pair formation, has also been a subject of AI modelling. Six ML algorithms were evaluated: Support Vector Machine (SVR), Random Forest, Kernel Ridge, Gaussian process regression, Gradient Boosting (GBoost), and Artificial Neural Networks (ANN) to predict T_c up to 100 GPa based on 584 structures characterised by λ and ω_{log}, which are the key parameters of electron-phonon interactions[14]. These models achieved MAE ≈ 3 K, demonstrating reliable high-pressure T_c prediction when incorporated in 3D crystal-structure information alongside chemical composition and XGBoost algorithm[15]. Structural descriptors improved the mean squared logarithmic error on untrained samples from 1.176 to 1.085. In a related effort, a dataset of 200,000 compounds with density-functional-theory-derived electron–phonon and superconducting properties was used to identify numerous candidate high T_c materials. The synergy between machine learning (ML) and first-principles calculations offers a systematic approach to exploring multiple phase diagrams and searching for potential room-temperature superconductors, yielding an estimated mean T_c = 7.63 K and MAE = 2.94 K [16] are yielded.

Using *ab initio* descriptors derived solely from electronic and atomic properties of constituent elements, have shown that electronegativity and electron concentration allow substantial dimensionality reduction[17]. The best-performing model, XGBoost, achieved R^2 = 0.92 and a T_c prediction accuracy of 93 %, MAE = 4.2 K. In Fe-based superconductors, where T_c strongly correlates with lattice parameters, the neural network model reached 91.2 % accuracy. It was used to predict T_c based on general theory of superconductivity applying ML using a random forest (RF) model informed by key material features such as thermal-conductivity range, weighted geometric-mean thermal conductivity, density variation, and valency descriptors[18,19]. Their best predictions were obtained for compositions with a fewer number of chemical components. Finally, to enhance predictive accuracy, high-throughput first-principles materials data were incorporated from the AFLOW Online Repository with RF regression models, achieving average R^2 = 0.88 [22]. Their model was subsequently applied to the Inorganic Crystal Structure Database (ICSD) to identify potential new superconductors, revealing more than 30 non-cuprate and non-iron-based oxide candidates.

Data

In this work, causal AI modelling and counterfactual propositions were based on the "Superconductivity Data" dataset available in the open-access machine-learning repository at the University of California, Irvine (UCI)[6]. The dataset comprises 21,263 tested materials, for which elemental chemical compositions (chemical formulae) and 81 modelling descriptors (features) are provided, including the number of chemical elements and the superconducting critical temperature, T_c. The dataset includes materials composed of 77 chemical elements. The average "pseudo"

chemical formula is $O_{0.29}Cu_{0.12}Ba_{0.054}Nb_{0.042}C_{0.037}$, accounting for 70 % of elemental composition, and yielding the average "pseudo" critical temperature, T_c = 34.4 K. The modelling approach is based on aggregated (distributional) effects evaluated from individual atomic properties.

The following 9 atomic properties, denoted as *x*, were considered:

1) Atomic mass: total proton and neutron rest masses, in atomic mass units (AMU).
2) First ionisation energy: energy required to remove a valence electron, (kJ mol^{-1}).
3) Atomic radius: calculated atomic radius, in picometers (pm).
4) Density: density at standard temperature and pressure, (kg m^{-3}).
5) Electron affinity: energy required to add an electron to a neutral atom, (kJ mol^{-1}).
6) Heat of fusion: net energy change required for solid to liquid transition at constant temperature (kJ mol^{-1}).
7) Thermal conductivity: thermal conductivity coefficient, (W m^{-1} K^{-1}).
8) Valence: typical number of chemical bonds formed by the element, no units.
9) Critical temperature T_c: superconducting critical temperature, (K).

For each material's elemental composition (chemical formula), interval distributions of atomic properties represented by the 10 statistical parameters (given in Table 1) are determined and applied as modelling features.

The samples of material atom descriptors form a large data-frame (matrix) comprising 21,263 rows and 82 columns (81 model descriptors plus T_c). The data are highly correlated, the first eigenvalue yielding 40 % and the first three eigenvalues yielding 60 % of the total variance. This fact is also confirmed by the principal component analysis showing that the first three components account for 60 % variance. The aim of this work was not to derive an AI machine-learning predictive model, but rather to infer causal effects between atom elemental composition descriptors and the critical temperature in the absence of explicit information on the crystal structure of the materials.

Table 1 – *Modelling descriptors (features) of physical property interval distributions, x, derived from elemental chemical composition*

	Modelling descriptor	Statistics of interval distribution of *x*
1	Mean	$\frac{1}{N}\sum_{i=1}^{N} x_i$
2	Weighted mean	$\sum_{i=1}^{N} p_i x_i$
3	Geometric mean	$\sqrt[N]{\prod_{i=1}^{N} x_i}$
4	Weighted geometric mean	$\prod_{i=1}^{N} x_i^{p_i}$
5	Shannon entropy	$-\sum_{i=1}^{N} p_i \ln(p_i)$
6	Weighted Shannon entropy	$-\sum_{i=1}^{N} A_i \ln(A_i) \quad A_i = p_i x_i \,/\, \sum_{i=1}^{i=N} p_i x_i$
7	Range	$x_{max} - x_{min}$
8	Weighted range	$p_{max} x_{max} - p_{min} x_{min}$
9	Standard deviation	$\sqrt{\frac{1}{N}\sum_{i=1}^{N} (x_i - \overline{x})^2}$
10	Weighted standard deviation	$\sqrt{p_i \sum_{i=1}^{N} (x_i - \overline{x})^2}$

Notes: Chemical elemental composition (chemical formula): $C_{\alpha 1}^{1} C_{\alpha 2}^{2} \cdots C_{\alpha N}^{N}$; C^i = *i*-th chemical element; *N* = number of chemical elements; p_i = probability of *i*-th element molar contribution: $\alpha_i \,/ \sum_{i=1}^{N} \alpha_i$; *x* = physical property.

Modelling

Modelling superconductivity as a macroscopic quantum effect based on fundamental laws is mathematically and numerically demanding. An alternative "short cut" methodology (data "mining") based on a large dataset and artificial intelligence (AI) algorithms is proposed to facilitate the discovery of new materials. The large UCI superconductivity dataset was applied, which provided material chemical compositions and corresponding T_c values. However, the dataset did not include key experimental variables such as sample preparation conditions, crystal or polycrystalline structural information, potential presence of impurities, confidence intervals of T_c, or reproducibility data from repeated experiments or independent sources (laboratories). Despite these limitations, the large sample size justified the assumption of potentially valid statistical inference. In view of data modelling by machine learning, data aggregation using interval-based "symbolic" fea-

tures was applied before analysis of causal patterns between atomic property distributions and T_c. The main reason for the application of interval-based "symbolic" features was to achieve averaged effects associated with unobserved and unknown factors, while also achieving a significant dimensional reduction of the sample space. Consequently, the large original dataset was transformed into a numerically manageable representation of interval-based dataset. The interval data samples were mapped into a reproducing kernel Hilbert space (RKHS) of infinite dimensionality using a Gaussian reproducible kernel. This mapping allowed the application of linear methods to discover nonlinear functional dependencies and causal directed acyclic graph (DAG) structures.

Interval "symbolic" features are generated through subsetting and binning of the 81 atomic property distribution features, $x \in [x_k, x_{k+1}]$ corresponding to the k-th temperature interval $T_c \in [T_{ck}, T_{ck+1}]$. This provides a comprehensive "bird's-eye view" of the materials by representing distributions of atomic properties as symbolic variables. Aggregation into interval features within RKHS results in a smaller and more manageable yet information-preserving dataset[21–23]. Importantly, representing interval data in RKHS enables the application of linear statistical inference for nonlinear dependencies present in the original Cartesian space. In this work, a Gaussian kernel k_x (radial basis function) was applied for mapping data from the original feature space of dimension R^N to a corresponding feature representation $\varnothing$ in an infinite-dimensional Hilbert space $\mathcal{H}^\infty$:

$$k_x\left(x_i, x_j\right) = \exp\left(-\left\|x_i - x_j\right\|^2 / h^2\right) \tag{1}$$

where x_i denotes the i-th sample (material) with N=81 component vector of features, and h is a data-dependent bandwidth kernel parameter[24–26]. This allows the use of the "RKHS trick" for the replacement of explicit numerical evaluation of inner scalar product in RKHS by kernel evaluation of original data in R^N:

$$k\left(x_1, x_2\right)_{R^N} = <\varnothing\left(x_1\right), \varnothing\left(x_2\right)>_{\mathcal{H}^\infty} \tag{2}$$

This implicit operation enables the application of kernel methods for the efficient analysis of complex data relationships and facilitates the effective recognition of patterns in infinite dimensional RKHS through computation in R^N dimensional finite space. Mapping of input data $X(n, p)$, where n is the number of samples and p is the number of observed features, yields Gram matrix $K(n,n)$ of Gaussian weights

$$\left(K_x\right)_{i,j} = k\left(x_i, x_j\right) \tag{3}$$

Modelling of nonlinear functional relations $f(x)$ in RKHS is enabled by the representer property:

$$f\left(x\right)_{R^N} = <f, k\left(\cdot, x\right)>_{\mathcal{H}^\infty} \tag{4}$$

evaluated as linear ridge regression. Basic statistical application of data mapping to RKHS is the nonparametric inference of probability density function $P(x)$ denoted as kernel density estimation, KDE

$$P\left(x\right) \approx \mathrm{KDE}\left(x\right) = \frac{1}{N}\sum_{i=1}^{N} k\left(x_i, x\right) \tag{5}$$

From the viewpoint of causal analysis, the most important result of mapping data to Hilbert space is the nonparametric evaluation of statistical inference of independence (HSIC, Hilbert Schmidt Independence Criterion between potentially nonlinearly-dependent variables X and Y. It is evaluated as a covariance of the corresponding Gram matrices K_x and K_y

$$\mathrm{HSIC}\left(X, Y\right) = \left\|C_{X,Y}\right\|^2_{\mathcal{H}} \approx \frac{1}{\left(N-1\right)^2}\mathrm{tr}\left(K_x H K_y H\right) \tag{6}$$

where H matrix enables centralisation of the Gram matrices. The main objective of causal data mining is the discovery of the structure of significant directed causal relations between data, DAG. This is a complex problem which is solved in two steps. Firstly, DAG skeleton is determined based on the PC (Peter and Clark) conditional dependence test dHSIC (d-variable HSIC), by testing independence (orthogonality) with nonparametric conditional covariance in RKHS[24].

$$\mathrm{HSIC\ test}\left[X_i \perp X_j \mid X_{-(i,j)}\right] \tag{7}$$

In the second step, the edges are oriented based on the Kolmogorov conjecture of causality from the complexity of nonparametric kernel-based model data predictions, i.e. by assuming that a correctly causally oriented model "better" explains observed data[28]. The Pearson correlations r between conditional nonparametric kernel-based model predictions $r(y, y_{\mathcal{H}}(x \mid z))$ and a $r(x, x_{\mathcal{H}}(y \mid z))$ conditioned with z confounding covariates are compared:

$$X \to Y \quad \Rightarrow \quad r\left(y, y_{\mathcal{H}}\left(x \mid z\right)\right) > r\left(x, x_{\mathcal{H}}\left(y \mid z\right)\right) \tag{8}$$

The inferred causal DAG is a Bayesian causal network allowing for deduction of causal pathways from a cause variable X to a target effect Y. Its deduction is based on d-separation of confounding variables responsible for adjustments of Simpson's paradox and elimination of collider variables which are the cause of prediction model Berkson's fallacy[29,30]. d-Separation modifies an initial DAG by closing all "back door" edges leading to the cause, removing mediators on the pathway from X to Y, and removing collider nodes. The obtained d-sepa-

rated causal network enables evaluation of the causal probability of "doing" distribution of target, $P(Y \mid \mathrm{do}(X = x))$, when the cause is deliberately set to a specific value, $X = x$, and averaging E_Z due to perturbation effects of the causally adjusted set of covariates Z:

$$P(Y \mid \mathrm{do}(X = x, Z)) = E_Z(Y \mid X = x, Z) \quad (9)$$

A validated causal model allows for the *a posteriori* prediction of hypothetical counterfactual effects. For i-th individual observed effect $Y{=}Y_{i,\mathrm{observed}}$ caused by $X{=}x_i$, the causal model yields the prediction $Y_{i,\mathrm{model}}$ of the case-specific unobserved exogenous influence e_i:

$$y_{i,\mathrm{observed}} = y_{i,\mathrm{model}}(X = x_i, Z = z_i) + e_i \quad (10)$$

Prediction of a hypothetical effect of the cause when changed from x_i to $\hat{x}_i$, under the observed specific conditions, is given by:

$$y_{i,\mathrm{hypothetical}} = y_{i,\mathrm{model}}(X = \hat{x}_i, Z = z_i) + e_i \quad (11)$$

A validated causal model and a counterfactual prediction algorithm may provide essential support in the experimental search for new superconductivity materials.

Results and discussion

To account for large-dataset aggregation, as well as the averaging of experimental errors and unobserved factors, the original dataset is transformed into symbolic features using temperature-interval binning. For samples with critical temperature above the boiling point of liquid nitrogen (T_c > 77 K), the dataset was reduced from X[3895, 82] to X[547, 82]. To assess the potential loss of information by interval aggregation, the probability density functions of the observed temperatures, $P_{\mathrm{observed}}(T_c)$, and the interval-averaged temperatures $P_{\mathrm{interval}}(T_c)$ were compared. For this purpose, kernel density estimation (KDE), defined in Eq. (5), was applied, and the resulting distributions are shown in Fig. 1. The results indicate that neither the substantial reduction in dataset size nor the averaging effects introduce significant distortions in the probability densities. This supports the hypothesis of using interval-based dataset for developing predictive and causal AI models linking material atomic properties and superconductivity critical temperature T_c.

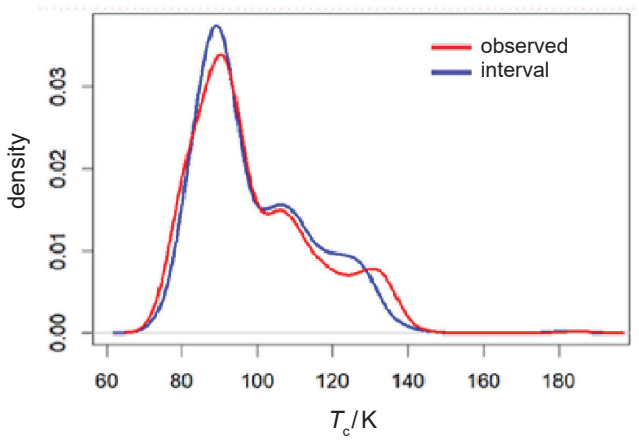

Fig. 1 – *KDE estimates of the probability density functions of critical temperature T_c> 77 K for the observed data (red) and of the interval symbolic data (blue)*

Table 2 – *Comparison of prediction accuracy for critical temperature, T_c obtained using machine-learning models based on the observed dataset (21,263 materials) and models based on the aggregated temperature-interval ("symbolic") dataset (547 samples)*

Machine-learning model	Observed data		Interval data	
	train/K	test/K	train/K	test/K
Random Forest	4.12	10.01	4.02	12.42
Extreme Gradient Boosting	4.17	8.88	4.94	12.39
Gradient Boosting	6.07	8.49	5.79	13.85
K-Nearest Neighbour	5.57	9.40	7.43	13.49
Ordinary Least Squares	5.75	9.26	6.31	13.14
Linear K-Nearest Neighbour	5.17	9.55	6.16	12.88
Generalised Random Forest	4.70	9.44	5.93	13.80
LASSO Least Absolute Shrinkage and Selection	5.78	8.84	6.09	14.35
Polynomial LASSO	5.80	9.65	6.74	14.71

Further evidence supporting the use of symbolic (interval-based) data was obtained by comparing the prediction errors of several linear and machine-learning algorithms (Table 2). The data were randomly split into training (80 %) and test (20 %) sets. For the observed dataset with 21,263 samples, the average prediction errors across all tested models were MAE(T_c) = 5.23 ± 0.74 K for the trained samples, and MAE(T_c) = 9.28 ± 0.47 K for the test samples. Using the interval-based symbolic features, the prediction errors were MAE(T_c) = 5.53 ± 0.08 K for trained samples, and MAE(T_c) = 13.45 ± 0.81 K for untrained samples. The most accurate predictions were achieved with Random Forest model, which achieved R^2 = 92.75 % on the training data and R^2 = 92.71 % on the test data. The observed increase in average prediction error for interval-based models from approximately 9.3 K to 13.4 K can be attributed to the ten-fold reduction in sample size between the symbolic interval dataset and the original observed data. Table 2. gives mean absolute errors in prediction by various machine-learning models evaluated for the training and test data for all the observed and interval data. Fig. 2 depicts predictions obtained by the Random Forest model.

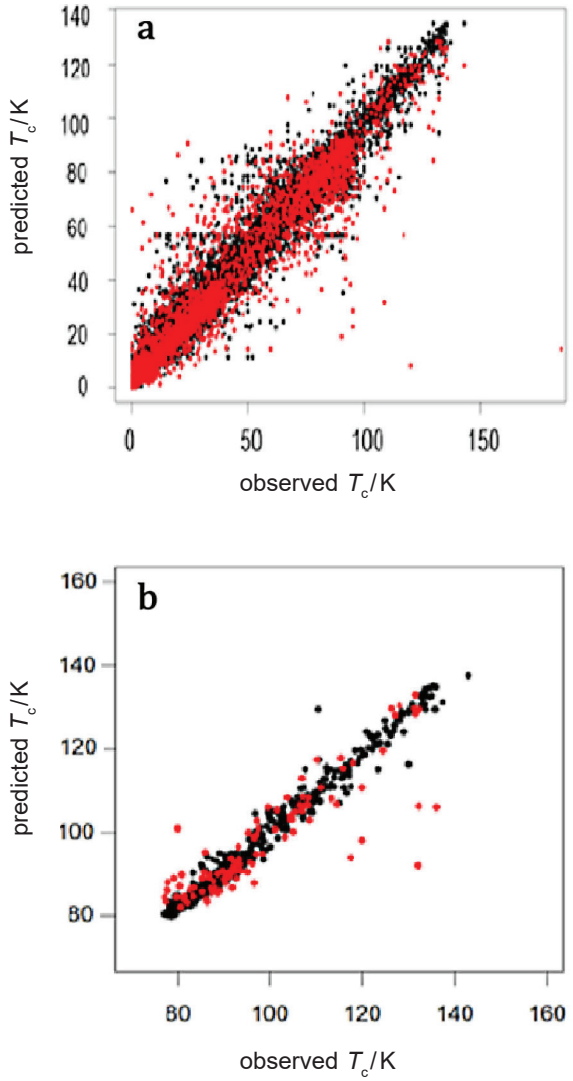

Fig. 2 – *Depiction of observed critical temperatures T_c (black dots) and Random Forest model predictions (red dots): (a) observed data, (b) symbolic interval data*

The obtained AI models show high accuracy for T_c predictions. However, because these models rely on a large and complete set of predictor variables (p = 81), they did not readily allow for transparent inspection of causal patterns. To investigate interactions among the predictors, the matrix of partial correlations was determined. Since the variables exhibited nonlinear relationships and their probability distributions were unknown, a nonparametric algorithm of distance partial correlations was applied to infer functional dependencies between predictors[31]. Euclidean distances were computed as matrices A and B of pairwise distances corresponding to two random variables x and y, defined as:

$$a_{j,k} = \left\| x_j - x_k \right\| \qquad j,k = 1,2,\ldots.N \qquad (12)$$

$$b_{j,k} = \left\| y_j - y_k \right\| \qquad j,k = 1,2,\ldots.N \qquad (13)$$

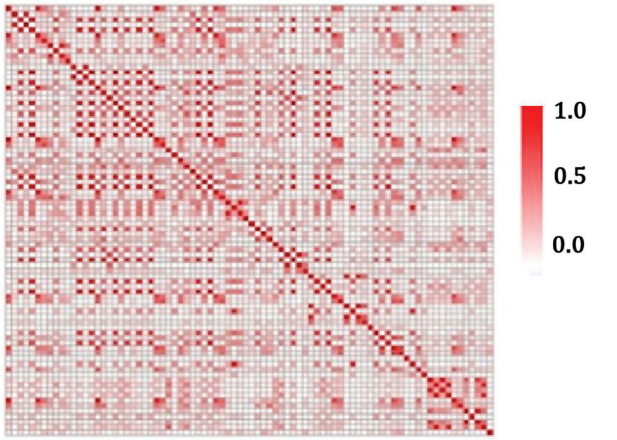

Fig. 3 – *Heat map of the partial distance correlation ("pdcor") matrix of the symbolic interval samples of 81 prediction features and T_c*

The matrices were centred by subtracting the corresponding row and column vector means from each matrix entry, followed by adding the global mean:

$$A_{j,k} = a_{j,k} - \bar{a}_j - \bar{a}_k + \bar{a}_j \qquad (14)$$

$$B_{j,k} = a_{b,k} - \bar{b}_j - \bar{b}_k + \bar{b} \qquad (15)$$

The distance covariance and distance correlation for N samples were calculated as the average sum of the corresponding $A_{j,k}$ and $B_{j,k}$ products of centred matrices A and B:

$$\mathrm{dcov}(X,Y) = \frac{1}{N^2}\sum_{j=1}^{N}\sum_{k=1}^{N} A_{j,k}B_{j,k} \qquad (16)$$

$$\mathrm{dcor}(X,Y) = \frac{\mathrm{dcov}(X,Y)}{\sqrt{\mathrm{dvar}(X)}\sqrt{\mathrm{dvar}(Y)}} \qquad (17)$$

To account for the effects of covariate predictors Z on X and Y, partial distance correlations based on residuals of regressions models, $\mathrm{residual}(X) = X - \sum \alpha_i Z_i$ and $\mathrm{residual}(Y) = Y - \sum \beta_i Z_i$, were evaluated:

$$\mathrm{pdcor}(X,Y \mid Z) = \mathrm{dcor}\begin{pmatrix}\mathrm{residual}(X \mid Z),\\ \mathrm{residual}(Y \mid Z)\end{pmatrix} \qquad (18)$$

Partial distance correlations are depicted as a heat map, as presented in Fig. 3.

The top ten partial distance correlations between critical temperature T_c and interval atomic properties are given in Table 3. The PC constraint-based algorithm was applied to uncover the structure of causal relationships. The structure (DAG) of interconnectivity between the variables was estimated using nonparametric PC algorithm with HSIC criteria for nonlinear dependencies be-

Table 3 – *Highest partial distance correlations (pdcor) between T_c and the interval symbolic features x*

Interval atomic property *x*	pdcor(T_c, *x*)
Weighted Shannon thermal conductivity	0.332
Geometric mean of electron affinity	0.327
Range of density	0.289
Weighted standard deviation of electron affinity	0.281
Entropy of thermal conductivity	0.275
Standard deviation of atomic density	0.258
Standard deviation of atomic mass	0.234
Weighted geometric mean of electron affinity	0.232
Range of atomic mass	0.186
Geometric mean of thermal conductivity	0.181

tween variables, and under the assumption of the presence of non-Gaussian exogenous unobserved factors (model noise)[32].

The first step in inferring the causal model structure was based on pairwise independence tests between variables *X* and *Y*, using the Hilbert–Schmidt independence criterion (HSIC; eqs. 6–7). The edges between network nodes (predictor variables) were removed using a permutation test at the significance level of α = 0.05. DAG stability was assessed by bootstrapping the data and averaging the resulting skeleton edges. In the second step, the edge orientations were assigned based on the complexity of causal conditional prediction (eq. 8). The resulting DAG was dense and only a subset (extended Markov blanket of T_c) is depicted in Fig. 4 highlighting the blanket of critical temperature T_c. The inferred DAG indicates that the direct causal effects on T_c arose from:

1. Standard deviation of atomic mass density,
2. Weighted geometric mean of atomic electron affinity,
3. Weighted geometric mean of atomic valence.

The functional dependence in the direct causal model is represented using the Random Forest model:

$$T_{\mathrm{c,causal\ model}} = \mathrm{RF}(x40, x45, x75) \qquad (19)$$

The predictions of critical temperature obtained by the causal model, $_{\mathrm{c,causal\_model}}$, for the complete dataset with 21,263 samples, are shown in Fig. 5a. The results demonstrate high accuracy, with only a negligible reduction in predictive performance compared to the agnostic Random Forest model using 81 predictors. The causal model's coefficient of determination was R^2=89.57 %, compared to R^2=92.71 % for the Random Forest models. The mean absolute prediction errors within the specified temperature ranges were MAE(T_c>77 K) = 5.1 K and MAE(T_c>0 K) = 4.6 K. To assess potential model biases, kernel density estimates (KDE) of the prediction errors were computed and are shown in Fig. 5b. The resulting symmetric and bell-shaped density functions exhibited Gaussian-like behaviour, which is consistent for unbiased predictions. Additional confirmation of the accuracy of the causal model was provided by the comparison of prediction errors from the agnostic and causal models for both training and test datasets summarised in Table 4.

A fundamental assumption in machine-learning modelling is that the training and test data are independent and identically distributed (i.i.d.), often described as "fair-coin" samples drawn from a time-invariant probability distribution. In practice, this assumption is rarely satisfied, especially when data originate from heterogeneous sources (e.g., many different laboratories) or are produced using diverse experimental methodologies. Because causal relationships are expected to remain invariant under changes in covariate distributions, a stringent test of a causal model is its predictive accuracy on out-of-distribution (OOD) data.

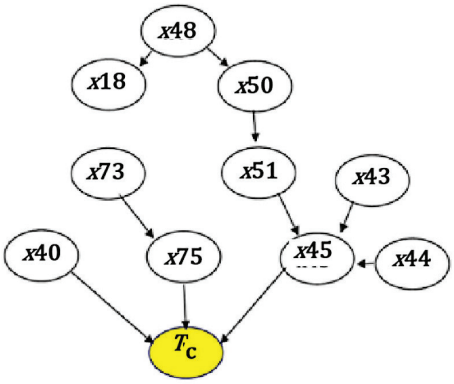

x48 Range of electron affinity
x18 Range of first ionisation energy
x50 Standard deviation of electron affinity
x73 Weighted mean valence
x51 Weighted standard deviation electron affinity
x43 Weighted mean electron affinity
x44 Geometric mean electron affinity
x40 Standard deviation of mass density
x75 Weighted geometric mean valence
x45 Weighted geometric mean electron affinity
T_c Critical temperature

Fig. 4 – *Subset of the directed acyclic graph (DAG) with Markov blanket for causal prediction of the critical superconductivity temperature T_c*

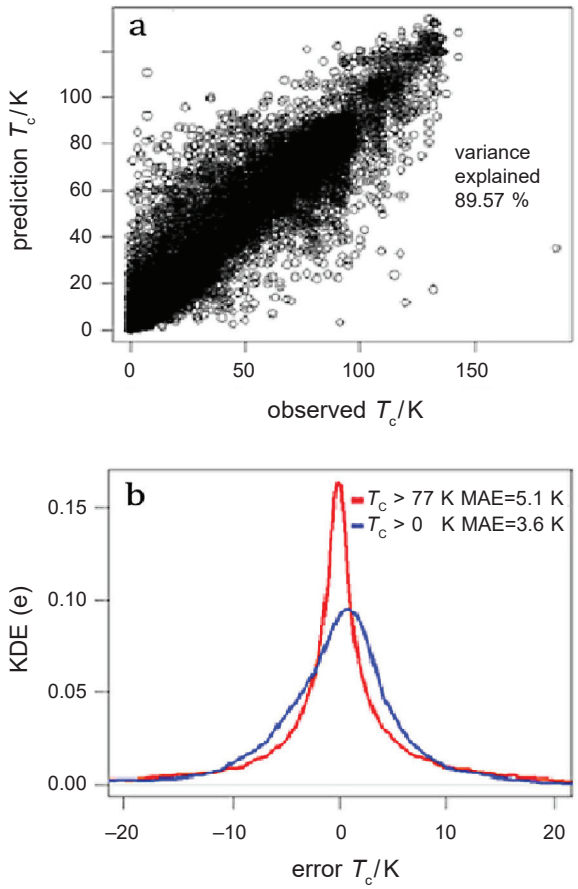

Fig. 5 – *a) Predictions of the critical temperature T_c by the causal model, b) kernel density estimation v(KDE) of prediction errors of the causal model*

Table 4 – *Comparison of the average prediction errors by the agnostic model with 81 predictor variables and the causal model with three direct causal factors validated by the random samples and the out-of-distribution (OOD) samples. The data include coefficient of determination, R^2, mean absolute error, MAE, and standard deviation, SD.*

	T_c [77 K–185 K]					
	Random sampled validation					
	Agnostic model			Causal model		
	R^2 %	MAE/K	SD/K	R^2 %	MAE/K	SD/K
Training	85.5	2.22	5.22	70.5	4.75	7.13
Test	77.4	4.01	5.85	70.6	4.74	6.54
	Out-of-distribution OOD validation					
Training	83.5	2.17	3.47	74.1	2.71	4.11
Test	76.9	5.81	8.48	77.9	2.92	4.35
	T_c [0 K–185 K]					
	Random sampled validation					
	Agnostic model			Causal model		
Training	92.5	5.22	9.31	89.7	6.78	11.48
Test	92.9	5.03	8.93	89.7	6.76	6.53
	Out-of-distribution OOD validation					
Training	94.5	2.54	4.88	93.9	2.78	5.38
Test	70.3	12.47	21.86	79.3	9.11	13.43

When information about experimental conditions is unavailable, OOD samples can be selected through data clustering, implemented here using the *k*-means algorithm[36]. The dataset, consisting of 21,263 samples and 81 features, was partitioned into 100 clusters, which were then randomly split into training (80 %) and test (20 %) subsets. The causal model was trained on the OOD training set and validated using the OOD testing set presented in Table 4. For samples with $T_c > 77$ K, the agnostic model had a coefficient of determination R^2= 31.9 % and MAE = 5.81 K, while the causal model yielded R^2 = 57.9 % and MAE = 11.1 K. For the complete set of OOD samples with $T_c > 0$ K, the agnostic model produced R^2 = 70.3 % and MAE = 12.47 K, whereas the causal model achieved R^2 = 79.3 % and MAE = 9.11 K. These results indicate that the causal model exhibited greater invariance to the effects of OOD covariate variability, suggesting enhanced robustness of the causal model under probability distribution perturbations.

The causal models are most useful when applied for inferring the causal effects of deliberate intervention actions X on Y in the presence of possible perturbations of Z cofactors. These interventions are named as statistics of "doing" effect and denoted by $Y(\mathrm{do}(X))$ [29,30]. Formally, numerical evaluation of $\mathrm{do}(X)$ function is the same as that in evaluating the partial dependence plot (PDP) for a causally adjusted model. In this case, the Bayesian neural network (BNN) was applied to gain insight into the probability distribution of nonlinear effects of the causal variables on critical temperature[33,34]. The parameters of a BNN network (weighting coefficients) are random variables yielding probabilistic effect on the network output.

$$T_c\left(\mathrm{do}\left(X = x\right)\right) = \mathrm{BNN}\left(x40, x45, x75\right) \quad (20)$$

The BNN model with a single hidden layer with 10 nodes and the sigmoid activation function were applied. Predictions of $T_c(\mathrm{do}(x))$ for standard deviation of atomic mass density, geometric mean atomic electron affinity, and weighted geometric mean of atomic valance are depicted in Fig. 6. The graphs show that the average effect of increasing standard deviation of atomic mass density was predominantly positive, while the effects of the weighted geometric mean atomic electron affinity and weighted geometric mean of atomic valence were negative. Average treatment effects (ATE), inferred as slopes

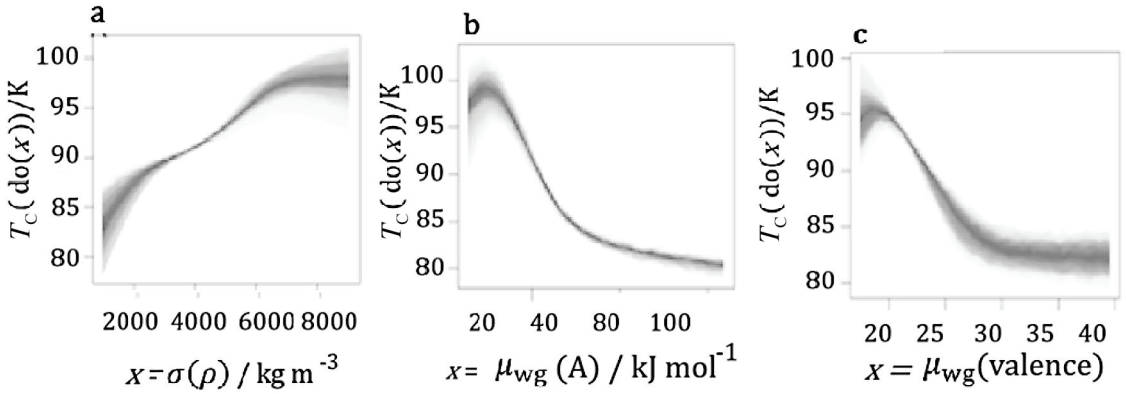

Fig. 6 – *Distributions of the direct causal effects on the critical temperature, T_c[do(x)], predicted by Bayesian neural networks BNN[x40, x45, x75]: a) standard deviation of atomic mass density x40=σ(ρ), b) weighted geometric mean atomic electron affinity x45=μ_{wg} (affinity), c) weighted geometric mean of atomic valence x75=μ_{wg} (valence)*

of the linear approximations of individual do(x) curves, were 0.005 K/(kg m^{-3}), –0.15 K/(kJ mol^{-1}) and 7.5 K for the standard deviation of atomic mass density, weighted geometric mean of atomic electron affinity, and weighted geometric mean of atomic valence, respectively. The obtained values were validated by comparison with predictions using General Random Forest (GRF) algorithm for nonparametric heterogeneous prediction[24,35]. The GRF method does not assume determination of causal DAG; however, it assumes un-confoundedness (negligible importance of unobserved dependencies), i.e., all confounders that affect both treatment and outcome were observed and included as covariates. The application of GRF yielded the average treatment effects of 0.007 K/(kg m^{-3}), and –0.22 K/(kJ mol^{-1}) for the standard deviation of atomic mass density, and weighted geometric mean atomic electron affinity, respectively. The estimates agreed with the causal structural model with an error within the acceptable interval of ±20 %. The validated causal model enabled counterfactual analysis based on the model predictions, *a posteriori* data and hypothetical assumptions of potential interventions. This corresponds to an analysis on the "third rung of the knowledge ladder"[29,30]. The following questions were raised here: what would be the effects on individual material (ICE, Individual Causal Effect) critical temperature T_c if the direct causal predictors were perturbed by ±10 %. The aim is to apply counterfactual inferences in experimental design studies for discovering improved and/or new superconducting materials. In addition, counterfactual analysis can be extended to infer average causal effects (ACE) for classes of supercritical materials, such as the cuprate family of materials composed of CuO_x layers alternating with layers of other metal oxides. For each individual superconducting material, the total exogeneous effect e_{exo} is inferred. For the cases presented here, this effect was due to unobserved and/or unaccounted intrinsic physical factors, random measurement errors, and modelling errors introduced by the RF(x40, x45, x75) model. The additivity of model prediction and exogeneous effect was assumed, as given by:

$$T_{c,\mathrm{observed}} = \mathrm{RF}(x40, x45, x75) + e_{exo} \tag{21}$$

The hypothetical individual causal effect (ICE) due to deliberate interventions by the simultaneous change of the direct causal factors for $\Delta_{40}, \Delta_{45}, \Delta_{75}$ was predicted by

$$T_{c,\mathrm{count.fact.}} = \mathrm{RF}(x40 + \Delta_{40}, x45 + \Delta_{45}, x75 + \Delta_{75}) + e_{exo} \tag{22}$$

ICE effects for various materials may significantly differ due to material-specific unaccounted causal factors and experimental procedures. The influence of these unexplained factors can be minimised by evaluation of a population average causal effect (ACE) for numbers of samples with common physical properties (e.g., for N cuprate materials) by:

$$\mathrm{ACE} = \frac{1}{N}\sum_{i=1}^{N} \mathrm{ICE}_i \tag{23}$$

The counterfactual ICE effects for three cuprate materials due to 10 % increase of x40 = standard deviation of atomic mass density, and 10 % decrease of x45 (weighted geometric mean electron affinity), and x75 (weighted geometric mean valence) are depicted in Fig. 7. Each hypothetical individual intervention resulted in a counterfactual increase of critical temperature T_c, while simultaneous perturbation of the three causal factors showed increases in T_c but also a sample with a negative synergy effect.

The numerical values of the counterfactual effects ICE and ACE for a set of cuprate superconductors are given in Tables 5 and 6. For individual materials, the positive and negative synergy effects were inferred, while for the population of the selected group of cuprate materials, the ACE effects exhibited a positive synergy mean increase of 10.46 K.

Table 5 – *Individual counterfactual effects (ICE) due to interventions of atomic property distributions. T_c is the observed superconductivity critical temperature, T_{c1} is due to 10 % increase in x40 (standard deviation of atomic mass density), T_{c2} is due to 10 % decrease in x45 (weighted geometric mean of electron affinity), T_{c3} is due to 10 % decrease in x75 (weighted geometric mean of valence), T_{c4} is the effect due to simultaneous intervention in x40, x45, and x75.*

Material	T_c/K	T_{c1}/K	T_{c2}/K	T_{c3}/K	T_{c4}/K
$Y_1Ba_2Cu_{2.94}Ni_{0.06}O_{7.01}$	85.0	84.78	84.04	91.31	87.77
$Gd_1Ba_{2.98}Zn_{0.02}O_7$	86.3	85.85	83.33	91.99	89.84
$Tm_1Ba_2Cu_{2.925}Fe_{0.075}O_7$	89.0	84.26	83.37	86.06	86.37
$Y_1Ba_2Cu_3O_{6.95}$	88.5	88.09	89.61	94.59	93.02
$Y_{0.6}Ca_{0.4}Ba_{1.8}Nd_{0.2}Cu_3O$	81.5	80.21	80.24	98.91	98.98
$Y_{0.8}Ca_{0.1}Pr_{0.1}Ba_2Cu_3O_{6.95}$	81.4	83.74	92.45	93.46	92.42
$Bi_2Sr_2Ca_{0.87}Pr_{0.13}Cu_2O$	88.9	94.23	84.13	90.86	96.17
$Hg_{0.76}Tl_{0.76}Ba_1Cu_1O_{4.5}$	87.5	99.78	101.87	116.51	103.59
$Bi_2Sr_2Ca_1Cu_2O_{8.16}$	85.0	94.16	95.63	104.24	110.24
$Ge_{0.5}Cu_{0.5}Sr_2Ca_{1.9}Y_{0.1}Cu_3O_{9.3}$	81.5	98.43	97.70	97.61	100.90
$Y_{0.9}Ca_{0.1}Ba_2Cu_4O_8$	89.0	87.86	83.57	90.14	88.15
$Bi_2Sr_{1.8}Ca_1Eu_{0.2}Cu_2O_{8.25}$	88.9	86.79	87.63	92.01	98.06
$Yb_{0.9}Pr_{0.1}Ba_2Cu_3O_{6.97}$	88.5	85.17	85.01	93.71	90.57
$Y_1Ba_{1.7}La_{0.3}Cu_3O$	83.2	89.71	84.86	103.75	100.73
$Tm_{0.9}Ca_{0.1}Ba_2Cu_3O_7$	86.0	87.06	84.37	85.16	95.25
$Y_{0.9}Ca_{0.1}Ba_{1.8}La_{0.2}Cu_3O_{6.97}$	87.0	84.35	83.06	91.42	90.64
$Y_1Ba_{1.4}Sr_{0.6}Cu_4O_8$	80.5	86.03	82.68	91.01	91.04
$Bi_2Sr_2Ca_{0.9}Na_{0.1}Cu_2O_8$	81.0	91.75	92.45	98.73	106.90
$Pb_{0.38}Bi_{1.75}Sr_{1.75}Ca_{1.1}Cu_2O$	87.0	89.81	99.65	104.85	102.19
$Y_{0.9}Pr_{0.1}Ba_2Cu_3O_{6.82}$	82.0	88.10	89.69	96.10	94.11

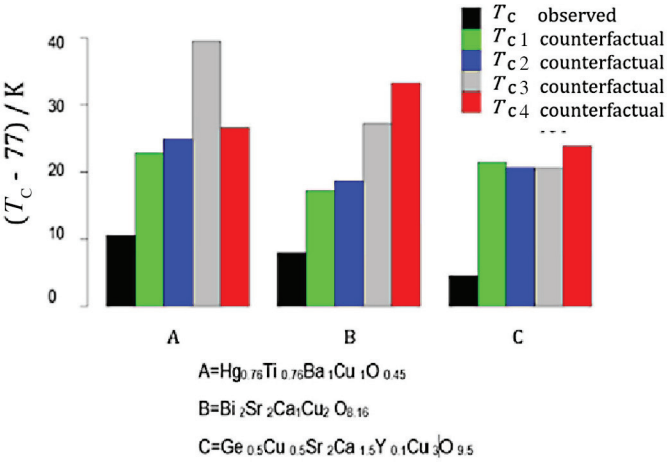

Fig. 7 – *Counterfactual individual causal effects (ICE) on superconductivity critical temperature: T_{c1}, induced by the 10 % increase in x40 (standard deviation of atomic mass density), T_{c2} induced by the 10 % decrease in x45 (weighted geometric mean of electron affinity), T_{c3} induced by the 10 % decrease in x75 (weighted geometric mean of valence), T_{c4} induced by simultaneous interventions*

Conclusions

Given the exponential growth of AI development followed by the extremely high energy consumption of large data centres, and also due to the global imperative for transition to a zero-carbon economy, the search for industrially viable superconducting materials has become increasingly important. Superconductivity is by nature a fundamental macroscopic quantum phenomenon and is extensively investigated in physics and materials science. However, because of the complex interactions between quantum-mechanical behaviour, chemical composition, and structural properties, it remains a challenging and still an open research field.

This work presents an alternative data-driven approach that integrates the large UCI dataset on materials superconductivity with causal AI modelling in a reproducing kernel Hilbert space (RKHS). To reduce sample dimensionality and the size of the associated Gram matrix, the UCI data were aggregated into "symbolic" interval features defined over ranges of superconductivity critical temperature, T_c. Besides reducing the dimensionality of the Gram matrix, the applied aggregation procedure averaged out sample preparation, presence of sample impurities, experimental measurement noise, confounding interactions, and unobserved latent (structural or quantum) factors.

Table 6 – *Average counterfactual causal effects (ACE) on the superconductivity critical temperature T_c induced by the hypothetical interventions for a set of cuprate superconductors*

	ACE/K, average causal effects		
	min	max	mean
*x*40 (standard deviation of atomic mass density) (+10 %)	–4.74	16.93	3.12
*x*45 (weighted geometric mean of electron affinity) (–10 %)	–5.63	16.2	2.88
*x*75 (weighted geometric mean of valence) (–10 %)	–2.94	29.01	10.24
Simultaneous interventions (+10 % +*x*40, –10 % *x*45, –10 % *x*75)	–2.63	25.9	10.46

The primary goal of this research was to infer a Bayesian causal network among 81 interval-valued atomic descriptors and critical temperature. The problem was addressed in two stages: (i) learning the network skeleton, and (ii) inferring orientation of the edges. Because the dependencies were strongly nonlinear, the skeleton was estimated using a constrained PC algorithm with HSIC criteria, while inference of the edge orientations followed the Kolmogorov conjecture of causality based on nonparametric kernel conditional modelling in Hilbert space. The inferred structural causal model (SCM) identified three direct causal predictors of T_c: the standard deviation of mass density, the weighted geometric mean of electron affinity, and the weighted geometric mean of valence.

The agnostic random-forest model using all 81 predictors achieved R^2=92.5 % and MAE=2.69 K, while the SCM using only the three causal features attained R^2=89.7 % and MAE=3.97 K. The superior robustness of the SCM was further confirmed by the evaluations on out-of-distribution (OOD) test sets, showing higher coefficients of determination and lower mean errors than the agnostic model. These results demonstrate the SCM's resilience to perturbations due to unobserved factors.

Nonlinear relationships between T_c and the causal predictors were modelled using Bayesian neural networks. The resulting "fan-plot" partial dependence plots characterised the probability distributions $P(T_c \mid X{=}x)$ of the do-effects. The dominant positive causal effect corresponded to the standard deviation of mass density (ATE = 0.105 K/(kg m^{-3})), while the weighted geometric means of electron affinity and valence exhibited negative effects of −0.15 K/(kJ mol^{-1}) and −7.5 K, respectively. These ATE estimates were independently confirmed by a general random-forest model within the error tolerance of 20 %.

Counterfactual analysis, based on the validated SCM, evaluated effects of hypothetical interventions in the three direct causal factors. Considering individual 10 % increases in the standard deviation of mass density and −10 % changes in the weighted geometric means of affinity and valence, as well as joint perturbations, the model predicted an average population-level increase of approximately 10.46 K across a tested group of 20 cuprate materials.

In summary, the aggregation of a large superconductivity dataset into symbolic interval-based features and its embedding into RKHS, enabled the discovery of a Bayesian structural causal model with dramatically reduced dimensionality. The transition from 81 agnostic predictors to only 3 causal predictors was achieved without substantial loss of predictive accuracy. The prediction accuracy of the validated SCM agreed with the errors reported in the literature, and most importantly significantly narrowed the search space for improved or new materials design. Hence, the inferred causal SCM model enhanced interpretability and dimensionality reduction, which substantially improved the prospects for identifying new, industrially viable superconducting materials.

References

1. *Gibney, E., Castelvecchi, D.,* Groundbreaking quantum-tunnelling experiments win physics Nobel, Nature **646** (2025) 523. doi: https://doi.org/10.1038/d41586-025-03194-2
2. Wikipedia contributors. Superconductivity. In Wikipedia, The Free Encyclopedia. Retrieved November 2, 2025. https://en.wikipedia.org/wiki/Superconductivity
3. Editorial, The potential of superconducting electronics, Nat. Electron **8** (2025) 375. doi: https://doi.org/10.1038/s41928-025-01402-5
4. *Drury, A., Miller, M., Langemeier, K., Rizakos, D.,* Data center power crunch: Meeting the power demands of the AI era, Blog Global, 23 July, 2025. https://www.sustainability.com/insights/data-center-power-crunch-meeting-the-power-demands-of-the-ai-era/
5. *Yazdani-Asrami, M., Sadeghi, A., Song, W., Madureira, A., Murta-Pina, J., Parizh, M*., Artificial intelligence methods for applied superconductivity: Material, design, manufacturing, testing, operation, and condition monitoring, Supercond. Sci. Technol. **35** (2022) 123001. doi: https://doi.org/10.1088/1361-6668/ac80d8
6. *Hamidieh, K.,* A data-driven statistical model for predicting the critical temperature of a superconductor, Comput. Mater. Sci. **154** (2018) 346. doi: https://doi.org/10.48550/arXiv.1803.10260
7. *Roter, R., Dordevic, S. V.,* Predicting new superconductors and their critical temperatures using unsupervised machine learning, arXiv:2002.07266 [cond-mat.supr-con] (2020). https://arxiv.org/abs/2002.07266
8. *Le, T. D., Noumeir, R., Quach, H. L., Kim, J. H., Kim, J. H., Kim H. M.,* Critical temperature prediction for a superconductor: A variational Bayesian neural network approach, arXiv:2002.04977 [physics.data-an] (2020). https://doi.org/10.48550/arXiv.2002.04977
9. *García-Nieto, P. J., García-Gonzalo, E., Paredes-Sánchez, J. P.,* Prediction of the critical temperature of a superconductor by using the WOA/MARS, Ridge, Lasso and Elastic-net machine learning techniques, Neural Comput. Appl. **33** (2021) 17131. doi: https://doi.org/10.1007/s00521-021-06304-z
10. *Jung, S. G., Jung, G., Cole, J. M.,* Machine-learning predictions of critical temperatures from chemical compositions of superconductors, J. Chem. Inf. Model. **64** (2024) 7349. https://pubs.acs.org/doi/10.1021/acs.jcim.4c01137
11. *Moscato, P., Haque, M. N., Huang, K., Sloan, J., Corrales de Oliveira, J.,* Learning to extrapolate using continued fractions: Predicting the critical temperature of superconductor materials, Algorithms **16** (2023) 382. doi: https://doi.org/10.3390/a16080382
12. *Shams, F. A., Ratul, R. H., Naf, A. I., Samir, S. S. H., Abir, S. R., Faisal, F., Nishat, M. M., Hoque, M. A.*, A machine learning based investigative analysis for predicting the critical temperature of superconductors, EAI Endorsed Trans. AI Robot. **2** (2023) 1. doi: https://doi.org/10.4108/airo.3622

13. *Sizochenko, N., Hofmann, M.*, Predictive modeling of critical temperatures in superconducting materials, Molecules **26** (2021) 8. doi: https://doi.org/10.3390/molecules26010008
14. *Tran, H., Vu, T. N.,* Machine-learning approach for discovery of conventional superconductors, Phys. Rev. Materials **7** (2023) 054805. doi: https://doi.org/10.1103/PhysRevMaterials.7.054805
15. *Sommer, T., Willa, R., Schmalian, J., Friederich, P.,* 3DSC – A dataset of superconductors including crystal structures, Sci. Data **10** (2023) 816. doi: https://doi.org/10.1038/s41597-023-02721-y
16. *Cerqueira, T. F. T., Sanna, A., Marques, M. A. L.*, Sampling the materials space for conventional superconducting compounds, Adv. Mater. **36** (2024) 2307085. doi: https://doi.org/10.1002/adma.202307085
17. *Carral, A. D., Roitegui, M., Fyta, M.,* Interpretably learning the critical temperature of superconductors: Electron concentration and feature dimensionality reduction, APL Mater. **12** (2024) 041111. doi: https://doi.org/10.1063/5.0189714
18. *Hu, Z.*, Fe-based superconducting transition temperature modeling by machine learning: A computer science method, PLoS ONE **16** (8) e0255823. doi: https://doi.org/10.1371/journal.pone.0255823
19. *Matasov, A., Krasavina, V.,* Prediction of critical temperature and new superconducting materials, SN Appl. Sci. **2** (2020) 1482. doi: https://doi.org/10.1007/s42452-020-03266-0
20. *Stanev, V., Oses, C., Kusne, A. G., Rodriguez, E., Paglione, J., Curtarolo, S., Takeuchi, I.,* Machine learning modeling of superconducting critical temperature, Comput. Mater. **4** (2018) 29. doi: https://doi.org/10.1038/s41524-018-0085-8
21. *Billard, L., Diday, E.,* Symbolic Data Analysis: Conceptual Statistics and Data Mining, Wiley Series in Computational Statistics, John Wiley & Sons, Chichester, West Sussex, UK, 2007. doi: https://doi.org/10.1002/9780470090183
22. *González Císaro, S. E., Nigro, H. S.*, Symbolic data analysis: A paradigm for complex data mining?, Int. J. Signs Semiotic Syst. **3** (2014) 9. doi: https://doi.org/10.4018/ijsss.2014010101
23. *Rodriguez O.*, RSDA: R to Symbolic Data Analysis, (2025). https://doi.org/10.32614/CRAN.package.RSDA
24. *Hastie, T., Tibshirani, R., Friedman, J.*, The Elements of Statistical Learning: Data Mining, Inference, and Prediction, Second Edition, Springer, Berlin, 2017. http://www-stat.stanford.edu/ElemStatLearn
25. *Nosedal-Sanchez, A., Storlie, C. B., Lee, T. C. M., Christensen, R.*, Reproducing kernel Hilbert spaces for penalized regression: A tutorial, Am. Stat. **66** (2012) 50. doi: https://doi.org/10.1080/00031305.2012.678196
26. *S. Pereverzyev*, An Introduction to Intelligence Based on Reproducing Kernel Hilbert Spaces, Springer, Berlin, 2022. https://link.springer.com/book/10.1007/978-3-030-98316-1
27. *Kalisch, M., Buhlmann, P.*, Estimating high-dimensional directed acyclic graphs with the PC-algorithm, J. Mach. Learn. Res. **8** (2007) 613. http://jmlr.org/papers/v8/kalisch07a.html
28. *Kurtanjek, Ž.*, Kauzalna analiza u ekonometriji primjenom Hilbertovog prostora reproducirajućih jezgri, Croat. Rev. Econ. Bus. Soc. Stat. **11** (2025) 67. doi: https://doi.org/10.62366/crebss.2025.1.005
29. *Pearl, J.*, Causal inference in statistics: An overview, Stat. Surv. **3** (2009) 96. doi: https://doi.org/10.1214/09-SS057
30. *Pearl, J., Mackenzie, D.*, The Book of Why, Penguin Books, London, 2018.
31. *Szekely, G. J., Rizzo, M, Bakirov, N. K.*, Measuring and testing dependence by correlation of distances, Ann. Stat. **35** (2007) 2769. doi: https://doi.org/10.1214/009053607000000505
32. *Kalisch, M., Bühlmann, P.*, Estimating high dimensional directed acyclic graphs with the PC algorithm, J. Mach. Learn. Res. **8** (2007) 613. doi: https://doi.org/10.48550/arXiv.math/0510436
33. *Scott, S. L., Varian, H. R.*, Predicting the present with Bayesian structural time series, SSRN Electron. J. **5** (2014) 4. doi: https://doi.org/10.1504/IJMMNO.2014.059942
34. *Scott, S. L.*, BoomSpikeSlab: MCMC for Spike and Slab Regression, 2025. https://doi.org/10.32614/CRAN.package.BoomSpikeSlab
35. *Tibshirani, J., Athey, S., Sverdrup, E., Wager, S.*, GRF: Generalized Random Forests, 2025. https://doi.org/10.32614/CRAN.package.grf
36. *Maechler, M., Rousseeuw, P., Struyf, A., Hubert, M., Hornik, K.*, Cluster: Cluster Analysis Basics and Extensions, R package version, 2.1.8.1., 2025.